

A catastrophic charge density wave in BaFe_2Al_9

William R. Meier,^{*,†} Bryan C. Chakoumakos,[‡] Satoshi Okamoto,[†] Michael A. McGuire,[†] Raphaël P. Hermann,[†] German D. Samolyuk,[†] Shang Gao,^{†,‡} Qiang Zhang,[‡] Matthew B. Stone,[‡] Andrew D. Christianson,[†] and Brian C. Sales^{*,†}

[†]*Materials Science & Technology Division, Oak Ridge National Laboratory, Oak Ridge, Tennessee 37831*

[‡]*Neutron Scattering Division, Oak Ridge National Laboratory, Oak Ridge, Tennessee 37831*

E-mail: 4wm@ornl.gov; salesbc@ornl.gov

Abstract

Charge density waves (CDW) are modulations of the electron density and the atomic lattice that develop in some crystalline materials at low temperature. We report an unusual example of a CDW in BaFe_2Al_9 below 100 K. In contrast to the canonical CDW phase transition, temperature dependent physical properties of single crystals reveal a first-order phase transition. This is accompanied by a discontinuous change in the size of the crystal lattice. In fact, this large strain has catastrophic consequences for the crystals causing them to physically shatter. Single crystal x-ray diffraction reveals super-lattice peaks in the low-temperature phase signaling the development of a CDW lattice modulation. No similar low-temperature transitions are observed in BaCo_2Al_9 . Electronic structure calculations provide one hint to the different behavior of these two compounds; the d-orbital states in the Fe compound are not completely filled. Iron compounds are renowned for their magnetism and partly filled d-states play

a key role. It is therefore surprising that BaFe_2Al_9 develops a structural modulation at low temperature instead of magnetic order.

Keywords

Charge density wave, intermetallic, aluminide, first order, phase transition, magnetic susceptibility, resistance, x-ray diffraction, neutron diffraction, Mössbauer

This manuscript has been authored by UT-Battelle, LLC under Contract No. DE-AC05-00OR22725 with the U.S. Department of Energy. The United States Government retains and the publisher, by accepting the article for publication, acknowledges that the United States Government retains a non-exclusive, paid-up, irrevocable, world-wide license to publish or reproduce the published form of this manuscript, or allow others to do so, for United States Government purposes. The Department of Energy will provide public access to these results of federally sponsored research in accordance with the DOE Public Access Plan (<http://energy.gov/downloads/doe-public-access-plan>).

Introduction

Some crystalline materials experience rearrangements of their atomic structure when they are heated or cooled. These structural transitions are important in many technologies including hardening steel,² battery materials^{3,4} and next generation electronic devices.⁵⁻⁷ In addition, examining the details of the structural and property changes offers insights into the mechanisms at play and inspires design of new useful materials. A charge density wave is a curious variant of a structural transition.

A charge density wave (CDW) is a modulation of a material's atomic lattice that develops on cooling. This phenomenon is characterized not only by a periodic redistribution of electronic density (the charge density wave), but also a complementary static periodic displacement of the atoms. Critically, most CDWs have wavelengths distinct from the repeat

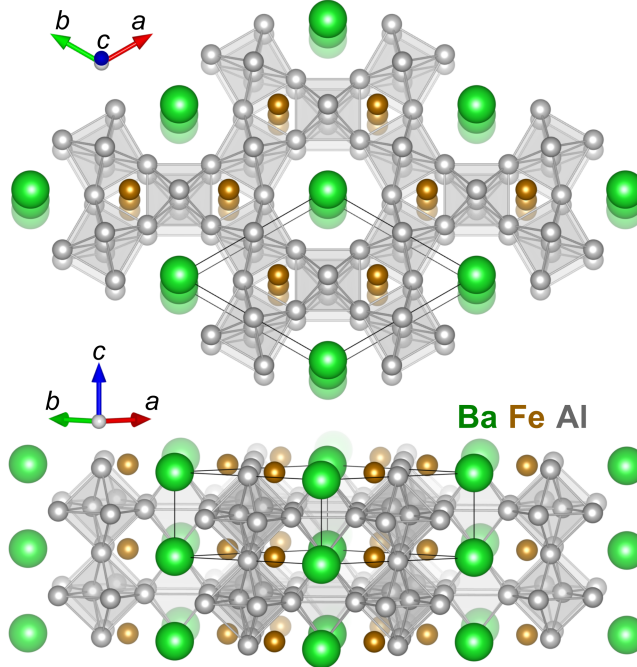


Figure 1: Crystal structure of BaFe_2Al_9 highlighting network of corner-sharing aluminum octahedra. Figures were generated in VESTA.¹

unit of the original crystal lattice.⁸ The simplest picture of a CDW is the Peierls model. Partially filled orbitals in a chain of atoms display an instability to forming alternating bonds.⁸⁻¹⁰ This is a powerful yet simple idea often used to understand dimers and distorted networks in a wide variety of chemical systems.¹¹⁻¹³ Although CDWs are usually introduced conceptually with the Peierls model, the origin of CDW order is not always clear.^{8,14-16}

CDW materials host unusual physical properties including metal-insulator transitions and nonlinear electrical conductivity.⁸ In addition, a number of CDW systems can be modified to suppress the modulation and induce superconductivity.^{17,18} CDW order has taken on new importance in the field of 2D materials like the transition metal dichalcogenides.¹⁸⁻²⁴ CDW modulations can modify the electronic, magnetic and optical properties of these materials in useful ways.²⁵⁻²⁸ Classic examples of CDWs occur in materials with 1D or 2D electronic structures derived from weakly-coupled chain-like ($\text{K}_{0.3}\text{MoO}_3$ and NbSe_3)^{8,29,30} or sheet-like motifs (NbSe_2 and EuAl_4).^{22,31-33} Few examples of 3D-network compounds with CDWs are known.¹⁴

BaFe₂Al₉ is a member of a family of aluminum-rich, intermetallic compounds; AM_2Al_9 . Turban and Schäfer introduced the family with BaM₂Al₉ ($M = \text{Fe, Co, Ni}$) and SrM₂Al₉ ($M = \text{Co, Ni}$).³⁴ CaCo₂Al₉³⁵ and EuCo₂Al₉³⁶ share the same structure and three indium-rich compounds are variations on the same theme; KCo₂In₉, KNi₂In₉³⁷ and BaIr₂In₉.³⁸ The hexagonal structure of BaFe₂Al₉ ($P6/mmm$ No. 191) is presented in Fig. 1.³⁴ First, note the 3D network of corner-sharing Al octahedra. Vajenine and Hoffmann discussed the network bonding in detail and noted that this aluminum framework provides some flexibility in the optimal electron count.³⁹ This likely explains why the structure forms with a series of transition-metals (Fe, Co, Ni) accommodating the additional electrons in the Al bands. Barium atoms are closely-spaced, forming columns along the c -direction within large channels in the Al-framework. The iron atoms are centered in a tri-capped triangular prisms of Al atoms. The nearest Fe-Fe (and Ba-Ba) spacings are unit cell height, c around 3.93 Å at room temperature.

BaFe₂Al₉ came to our attention while searching the ICSD for transition-metal materials with kagome-lattice motifs.⁴⁰ Although Al (not Fe) formed the desired lattice, the compounds still held an opportunity for interesting magnetism. Specifically, the Materials Project database predicted that the electronic structure had partially filled d-orbitals⁴¹ from the stacked honeycombs of Fe. To our surprise, BaFe₂Al₉ develops a CDW without any signs of the magnetism we anticipated.

We report a charge density wave below 100 K in crystals of BaFe₂Al₉ grown from an aluminum melt. Physical property measurements reveal that this transition is first-order with a sufficiently large change of the lattice parameters to shatter the crystals (0.5 and 1.5%). Single crystal x-ray diffraction resolves super-lattice peaks at low temperature signaling CDW order. In contrast, BaCo₂Al₉ has no phase transitions below room temperature. Electronic structure calculations reveal that the transition-metal d-orbitals are partly filled in BaFe₂Al₉ and completely filled in BaCo₂Al₉. Based on this comparison, we propose that d-electrons in the Fe compound play a key role in CDW formation. Iron is renowned for its magnetism and

partly filled d-orbitals are key to its behavior. This makes it more surprising that BaFe_2Al_9 hosts CDW order. This dramatic structural transition is the first CDW in an Fe-intermetallic compound and a rare example of a CDW in a 3D-network compound. BaFe_2Al_9 has many opportunities for chemical substitution to tune this transition to investigate its origin and its concomitant, large lattice contraction.

Experimental

Crystal growth

Crystals of BaFe_2Al_9 and BaCo_2Al_9 were grown from an aluminum-rich melt using a starting atomic composition of $\text{Ba}:M:\text{Al} = 6:8:86$ ($M = \text{Fe}$ and Co) in 1.5-2.1 g batches. Barium pieces (Alfa Aesar 99.9%), iron granules (Alfa Aesar 99.98%), cobalt powder (Alfa Aesar 99.8%) and aluminum shot (Alfa Aesar 99.999%) were loaded into a 2 mL alumina Canfield Crucible Set.⁴² The raw materials and crucibles were sealed in a fused silica ampoule filled with argon. In a box furnace, the assembly was heated to 1150 °C over 6 h, held for 12 h then slowly cooled to 1000 °C over 200 h to grow the crystals. The ampoule was removed from the hot furnace, inverted into a centrifuge and spun to remove the remaining Al-rich solution from the crystals.

Products

This procedure yielded around 0.5 g of metallic hexagonal crystals with habits ranging from needles to blocky columns 0.3-7 mm in diameter which often spanned the interior of the crucible (up to 13 mm long). Crystals of BaCo_2Al_9 were generally smaller and thinner. These brittle crystals exhibit conchoidal fracture with no evidence of cleavage. Flux on the crystal surfaces was dissolved away in a 1 M HCl solution over 0.5-4 h.

Characterization

Magnetization measurements were performed at 2 kOe on single crystals or crushed crystals in plastic drinking straws with a Quantum Design Magnetic Property Measurement System (MPMS) between 2 and 300 K using a rate of 1 K/min. 4-probe electrical resistance was measured on crystals contacted with Pt wire and Ag epoxy (EPO-TEK H20E) between 2 and 300 K (at 1 K/min) with the ac-transport option of a 9 T Quantum Design Physical Property Measurement System (PPMS). Small, previously shattered crystal fragments were more likely to hold together during resistance measurements. Heat capacity was measured using the Quantum Design heat capacity option of the PPMS using Apiezon N-grease between 1.8 and 200 K.

Powder neutron diffraction was performed using the POWGEN time of flight diffractometer at the Spallation Neutron Source at Oak Ridge National Laboratory.⁴³ 1.83 g of ground BaFe₂Al₉ crystals were held in a vanadium can in the POWGEN Automatic Sample Changer. Measurements were performed at temperatures from 7 to 300 K using neutron wavelength bands centered at 1.5 and 2.66 Å. Rietveld refinement was performed using Jana2020.⁴⁴

The lattice parameters were determined by powder x-ray diffraction (PANalytical X'pert Pro, with Cu-K α 1 radiation). An Oxford PheniX closed-cycle helium cryostat was used for scans below room temperature. Lattice parameters were determined from full 2θ scans taken at each temperature.

Single-crystal diffraction data were collected from a 100 μ m BaFe₂Al₉ crystal fragment as a function of temperature using a Rigaku XtaLAB PRO diffractometer with graphite monochromated Mo K α radiation ($\lambda = 0.71073$ Å, 50 kV and 40 mA) equipped with a Rigaku HyPix-6000HE detector and an Oxford N-HeliX cryocooler. Peak indexing and integration were done using the Rigaku Oxford Diffraction CrysAlisPro software.⁴⁵ An empirical absorption correction was applied using the SCALE3 ABSPACK algorithm as implemented in CrysAlisPro. Omega scans with counting times up to 60 s per point ensured that the weak superlattice reflections could be easily seen. Structure refinements were performed in

Temperature-dependent ^{57}Fe Mössbauer spectra were acquired on ground BaFe_2Al_9 crystals placed in a Janis SH-850 closed cycle cryostat. A 15 mCi ^{57}Co source and a Ritverc-2 Tl@NaI detector were used with a Wissel drive. This was calibrated using a room-temperature alpha-iron sample, which serves as a reference for the isomer shift. Data was acquired between 295 K and 10 K, first on cooling and then on heating to reveal the hysteretic nature of the transition.

DFT calculations were carried out using the projector augmented wave method⁴⁶ with the generalized gradient approximation in the parametrization of Perdew, Burke, and Enzerhof (PBE)⁴⁷ for exchange-correlation as implemented in the Vienna *ab-initio* simulation package (VASP).⁴⁸ For Ba, a pseudo-potential, in which semi-core s-states are treated as valence states, is used (Ba_{sv} in the VASP distribution). For Fe, Co and Al standard potentials are used (Fe, Co and Al, respectively). For both cases, we use the experimental lattice parameters obtained at room temperature with a $12 \times 12 \times 12$ \mathbf{k} -point grid and an E cutoff of 500 eV. Local Hubbard $+U$ correction is not included because both compounds are itinerant intermetallic systems. While the spin-orbit coupling was included, its effect is negligibly small because no heavy elements had states near the Fermi-level. In both cases, paramagnetic ground states are stabilized, consistent with experimental observations.

Results

Physical properties

Figure 2 presents the low temperature physical properties of BaFe_2Al_9 and BaCo_2Al_9 . In Fig. 2a, the Co compound shows a relatively small, paramagnetic susceptibility, χ , with weak temperature dependence across the whole temperature range. This is consistent with the Pauli paramagnetic response of a metal.^{49,50}

BaFe_2Al_9 has a similar flat magnetic response at high temperatures but the susceptibility

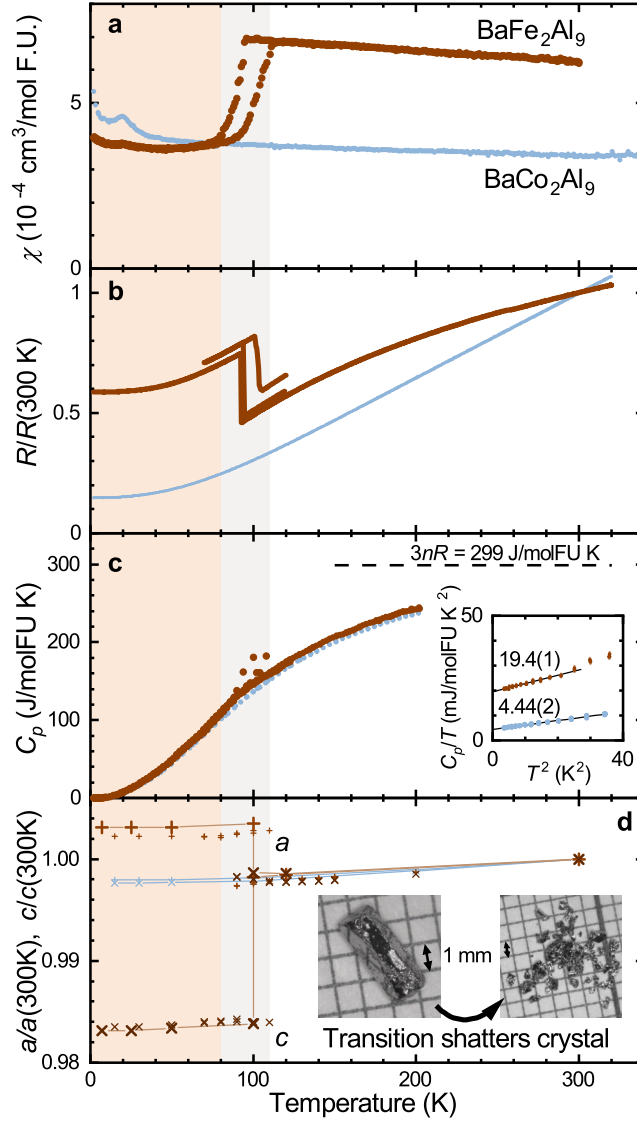


Figure 2: Physical properties of BaFe_2Al_9 (brown) and BaCo_2Al_9 (blue) reveal a first order phase transition in BaFe_2Al_9 . (a) Magnetic susceptibility measured at 2 kOe. (b) Electrical resistivity normalized to 300 K value. (c) Specific heat capacity and inset showing estimated γ in mJ/molF.U.K^2 . (d) Relative a (+) and c (\times) lattice parameters of BaFe_2Al_9 determined by powder neutron diffraction (big symbols) and powder XRD (small symbols). The BaCo_2Al_9 data was measured by powder XRD. The inset shows a BaFe_2Al_9 crystal before and after shattering during the phase transition.

rapidly decreases around 100 K on cooling. Below this, the χ is nearly temperature independent once again. This change in magnetic response occurs over a 10 K range and displays a 10 K hysteresis between heating and cooling. Both features are suggestive of a first-order phase transition in BaFe_2Al_9 at around 100 K. Neither compound has a significant Curie-Weiss contribution suggestive of local magnetic moments. The weak peak in both curves near 20 K is not present in all samples and is likely an impurity.

In Fig. 2b the electrical resistance of both compounds exhibit metallic behavior with resistance generally increasing with temperature. The data for BaFe_2Al_9 displays a conspicuous 60% jump around 100 K on cooling between two metallic regimes. This hysteretic feature coincides with the first order transition observed in the magnetization measurement. Although the orientation of the small BaFe_2Al_9 crystal used for this measurement is unknown, another sample had a resistivity of $144 \mu\Omega \text{ cm}$ along the c -axis at 300 K.

BaCo_2Al_9 shows uninterrupted metallic resistance down to base temperature with resistivity along the c -axis of 2.3 and $16 \mu\Omega \text{ cm}$ at 2 and 300 K, respectively. This results compares well with the resistance behavior reported by Rzyżyńska et al. although we observe a smaller residual resistance ratio of 6.7 instead of 10.⁵¹ Neither BaFe_2Al_9 or BaCo_2Al_9 display superconductivity above 1.85 K.

Figure 2c presents the low-temperature specific heat capacity of the two compounds. BaCo_2Al_9 exhibits a relatively featureless heat capacity curve. The BaFe_2Al_9 data have a slightly larger C_p across the whole range and a subtle change in slope near 100K. A first order transition would be expected to produce a spike at this temperature corresponding to the latent heat. Instead, we find a few data points with elevated values of C_p . These are likely due to the portions of the sample transforming at different times. The 10 K transition width observed in magnetic susceptibility also suggests an inhomogeneous transformation. This is likely why a single, sharp peak expected for a first-order phase transition is not observed near 100 K in the BaFe_2Al_9 specific heat data.

The inset of Fig. 2c shows fits to the lowest temperature specific heat data to estimate the

electronic heat capacity term, γ . We estimate values of 19.4(1) and 4.44(2) mJ/molF.U.K² for the BaFe₂Al₉ and BaCo₂Al₉, respectively. Rzyńska et al. calculated a γ of BaCo₂Al₉ to be 7.94 mJ/molF.U.K². Our estimated γ of the Fe compound is 4.4 times that of the Co variant suggesting a larger electronic density of states in the low temperature phase.⁵⁰ In contrast, the low temperature magnetic susceptibilities of the two compounds (Fig. 2a) suggest that they have comparable density of states below 100 K. Pauli paramagnetic and Landau diamagnetic contributions are proportional to the density of states and should be dominant in these two metals.⁵⁰ Therefore, similar χ values imply similar density of states. The origin of this contradiction is not clear, but the enhanced value of γ in BaFe₂Al₉ might arise from electronic correlations.

Figure 2d presents the temperature dependence of the lattice parameters of BaFe₂Al₉ and BaCo₂Al₉ determined by powder x-ray (small symbols) and neutron diffraction (larger symbols). BaCo₂Al₉ shows a relatively isotropic contraction of the lattice by 0.2% for both a and c between 300 and 15 K. This is in contrast to the anisotropic thermal expansion observed in isostructural BaIr₂In₉.³⁸ The thermal expansion of BaFe₂Al₉ shows a similar uniform lattice contraction down to 100 K. The lattice parameters change discontinuously at the transition observed in magnetization and resistance measurements. a abruptly increases by 0.5% and c shrinks by 1.5% for a net volume contraction of 0.5%. Coexistence of the high and low temperature phases is observed between 80 and 110 K in both the x-ray and neutron experiments. Phase coexistence and the jump in the lattice parameters provide further evidence that the transition in BaFe₂Al₉ is truly first order.

This inhomogeneous first-order transformation has catastrophic consequences for crystals of BaFe₂Al₉. Samples cooled through 100 K physically shatter. Crystals larger than 1 mm fragment into 0.01 - 0.3 mm pieces as depicted by the insets of Fig. 2d. This can be accomplished by dropping them in liquid nitrogen. This self-destructive behavior likely stems from the large, 1.5% strain at the transition. Rigid inclusions and an inhomogeneous transformation will develop significant stresses in samples causing them to fail. This unfortunate

feature of BaFe_2Al_9 complicated physical property measurements. Samples either had to be held together mechanically or had to be small enough that they survived the transformation.

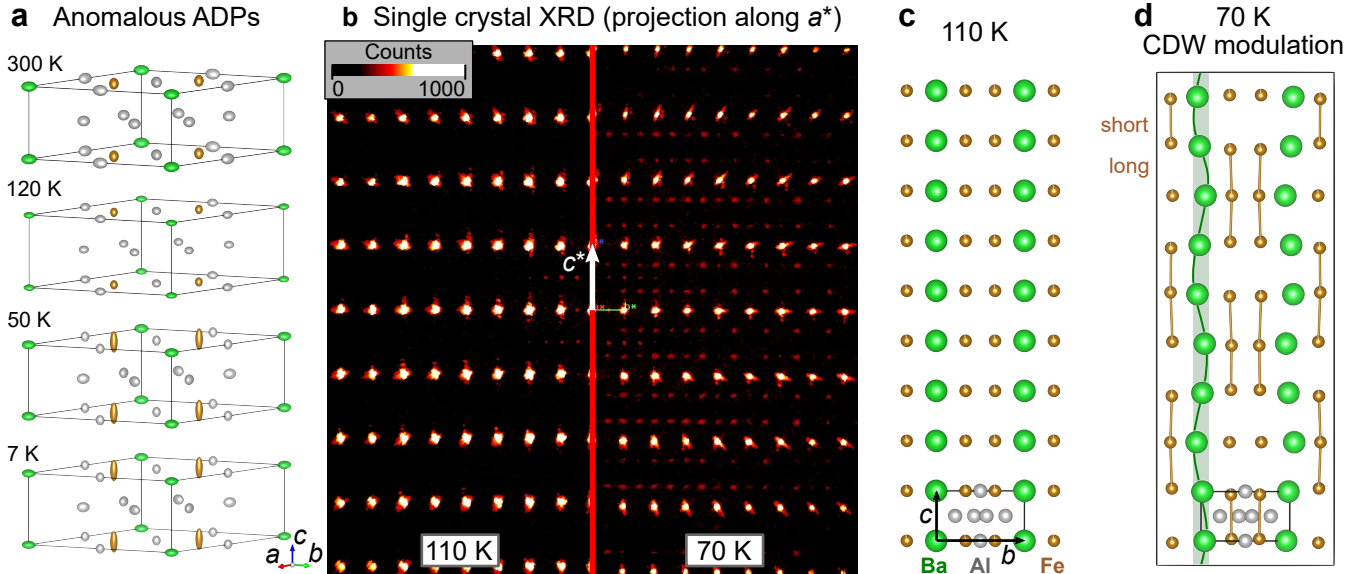


Figure 3: Evidence for a charge density wave (CDW) in BaFe_2Al_9 . (a) Atomic displacement parameters (ADP) from powder neutron diffraction (represented by 99% displacement ellipsoids) are anomalously large below 100 K suggesting a change in crystal structure. (b) Single crystal x-ray diffraction data with all intensity projected along a^* showing new super-lattice peaks at 70 K. The origin is at the center. Peaks at half-integer L near the origin at both temperatures are half-wavelength reflections. (c) Projection of BaFe_2Al_9 structure along the hexagonal a direction. (d) Depiction of the CDW structure showing Ba and Fe position modulations. Vertical links between Fe atoms denote shorter than average Fe-Fe distances to emphasize their vertical displacements.

Evidence for charge density wave

The temperature-dependent physical properties presented in Fig. 2 suggest that a first-order phase transition occurs in BaFe_2Al_9 around 100 K. Powder x-ray and neutron diffraction measurements did not reveal any evidence for new diffraction peaks, measurable deviations from hexagonal symmetry or magnetic order. Refinement of the neutron diffraction data revealed a dramatic increase in Fe and Ba atomic displacement parameters (ADPs) on cooling through 100 K (Fig. 3a and supplemental information). This increase was notably anisotropic; Fe atoms displace more along the $[001]$ direction and Ba in the ab -plane. This observation

signals a potential lattice modification in the low temperature phase.

We turn to single crystal x-ray diffraction to expose the nature of this phase transition. Figure 3b presents all the measured intensity in reciprocal space projected along the \mathbf{a}^* direction (i.e. projected onto the $(-H \ 2H \ L)$ reciprocal plane). At 110 K (left side) a rectangular array of peaks is observed consistent with the room-temperature $P6/mmm$ unit cell. At 70 K, new peaks appear signaling a change in lattice periodicity. These superlattice peaks are on the order of 1/300th the intensity of the primary reflections and can be indexed by three symmetry-related wave vectors: $\frac{1}{2}0 k_z$, $-\frac{1}{2}\frac{1}{2}k_z$, and $0-\frac{1}{2}k_z$. We determined the incommensurate index, $k_z = 0.3020(9)$ r.l.u. at 70 K. These peaks signal the presence of a charge density wave (CDW) modulation in the low temperature phase of BaFe_2Al_9 .

Using ISODISTORT, we determined that $P6/mmm$ has 4 irreducible representations with wave-vector $\frac{1}{2}0 k_z$.^{52,53} Among these, the U_4 displacement modes were consistent with anomalous Fe and Ba ADPs noted above and gave the best agreement with the superlattice intensities using Jana2020.

Figure 3c shows the refined 110 K hexagonal structure viewed along the a direction and Fig. 3d shows the corresponding view of our best model of the modulated CDW structure at 70K. This is a commensurate approximate version of the CDW with 20-times larger, C-centered orthorhombic unit cell (thin black rectangle) corresponding to the super-lattice wave-vector. First, note that straight columns of barium atoms at 110 K along the [001] direction develop a sine-modulated, horizontal displacement with a period of $\frac{10}{3}c$. The Fe atoms also have modulated displacements primarily along [001] leading to varying Fe-Fe distances. Lines connect Fe atoms that are closer than average emphasizing this change. These displacements correspond to the directions with large Fe and Ba ADPs in Fig. 3a at low temperature.

We are confident that the dominant distortion mode is similar to the one depicted in Fig. 3d and transforms at the U_4 irreducible representation. This model best explains the ADPs of the refined average structures and intensity of the superlattice peaks. Unfortunately,

our x-ray data does not provide a complete refinement of the modulated structure. Attempts to refine the modulated structure in Jana2020 yielded confident modulation parameters for the heavier Ba and Fe atoms but not for the two Al sites. Including these parameters did not give consistent or stable solutions and negative ADP parameters signaled that this model is insufficient to completely describe the data.

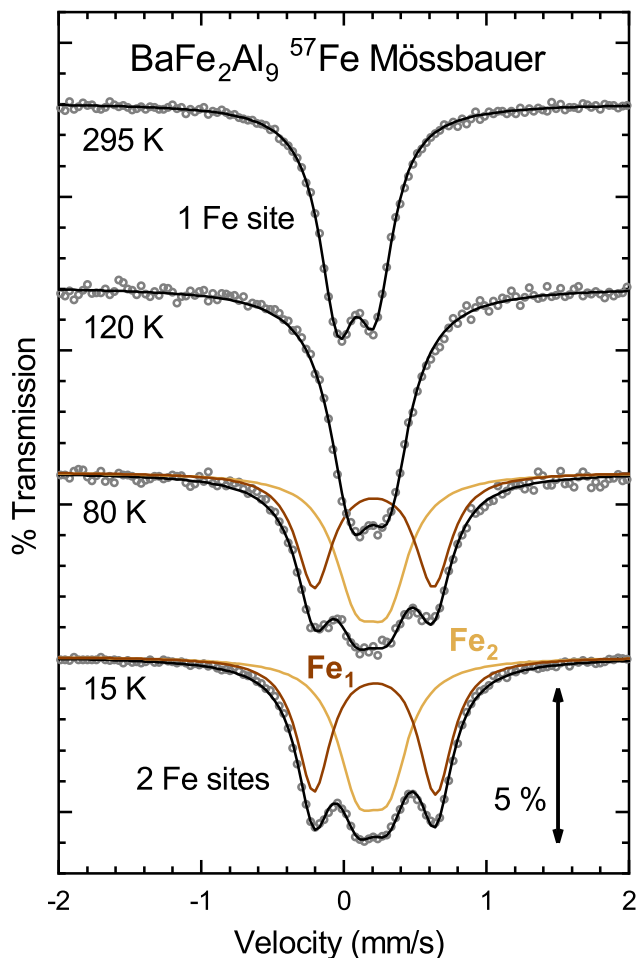


Figure 4: ^{57}Fe Mössbauer spectroscopy of powdered BaFe_2Al_9 shows an absorption doublet from the single Fe site in hexagonal BaFe_2Al_9 at 120 and 295 K. In the low temperature CDW phase (80 and 15 K) the spectra are best fit with two doublets corresponding to two distinct Fe sites.

In addition to our partial structure refinement, ^{57}Fe Mössbauer spectroscopy indicates that our CDW description in Fig. 3d is missing something. Figure 4 presents the Mössbauer spectra for BaFe_2Al_9 above and below the first order transition. At 295 and 120 K, a single

absorption doublet is observed generated by the single iron site in the room-temperature structure. The small asymmetry suggests a minor preferential orientation. The spectra change abruptly on cooling through the transition and four peaks can be resolved. This spectrum is best modeled by a pair of doublets as show. These correspond to two iron sites with different quadrupole splitting values and isomer shifts with equal population. In short, the low temperature phase of BaFe_2Al_9 has two types of iron atoms with different local environments. None of the measured spectra showed evidence of magnetic hyperfine splitting. Based on magnetic susceptibility, neutron diffraction, and this Mössbauer result, BaFe_2Al_9 does not appear to undergo magnetic ordering.

First, this Mössbauer evidence for two Fe sites at low temperature supports our identification of a structural change below 100 K. However, our diffraction result is not immediately consistent with two Fe sites. The first-order super-lattice peaks observed only provide information on the first harmonic of the position modulations. The simplest (sinusoidal) modulation this describes would give a distribution of iron site environments with a range of Mössbauer parameters, not two distinct Fe-site populations. The Mössbauer spectra are not well fit by such a distribution of quadrupole splittings and isomer shifts (see supplemental material).

There are likely higher-order harmonics to the CDW modulation which generate the two distinct Fe atom environments suggested by Mössbauer spectroscopy. These additional modulation components should generate higher-order super-lattice peaks.⁵⁴ We suspect these were too weak for us to resolve with the single crystal diffractometer. Between an inconclusive x-ray refinement and the Mössbauer result, the CDW structure of BaFe_2Al_9 presented in Fig. 3d is not yet a complete description of the low temperature structure.

Discussion

The temperature dependent physical properties in Fig. 2 reveal a first-order phase transition in BaFe_2Al_9 around 100 K which tends to shatter the crystals. Superlattice peaks observed with single crystal XRD reveal that the low temperature phase is a charge density wave. No such transition is observed in BaCo_2Al_9 . Electronic structure calculations provide one clue to why a CDW appears in the Fe and not the Co compound; the filling of the transition-metal d-orbitals.

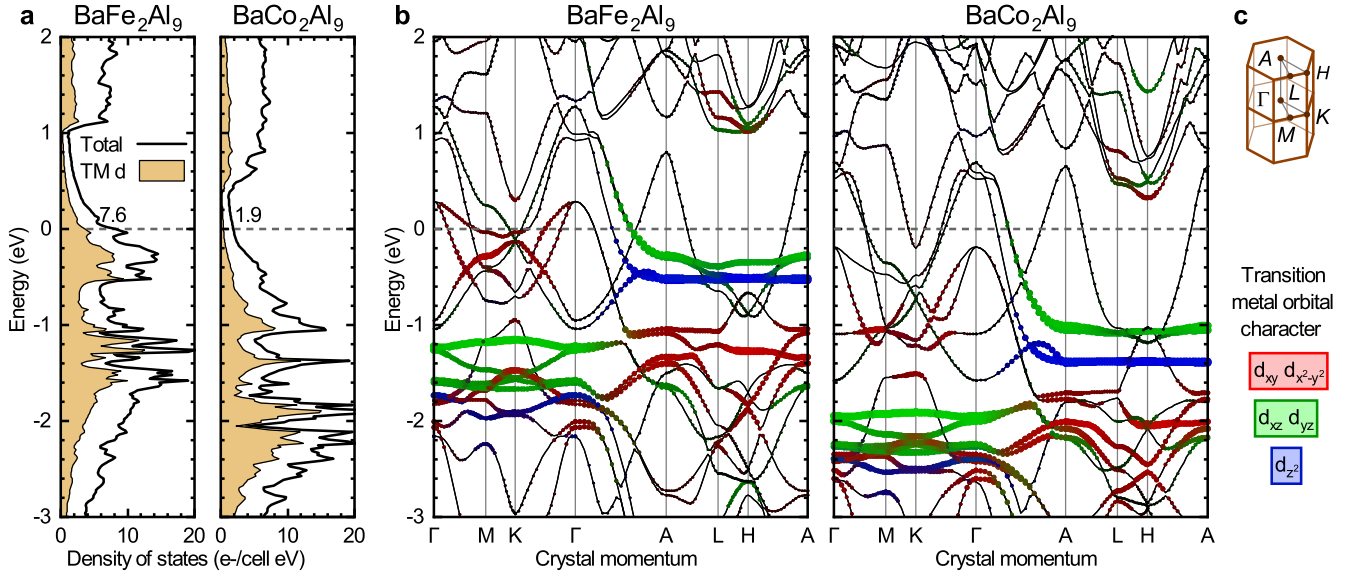


Figure 5: Electronic structures of BaFe_2Al_9 and BaCo_2Al_9 from density functional theory. (a) The electronic density of states for both compounds. The yellow fill represents the transition metal (TM) d-orbital contribution. The calculated density of states in electrons/unit cell eV sit above the Fermi level (dashed line). (b) The electronic band structure of the two aluminides. Thicker lines have more d-orbital character and the color represents contributions of specific d-orbitals. Note that the thicker d-bands are only partially filled in BaFe_2Al_9 . (c) Brillouin zone of BaFe_2Al_9 with momentum point labels.

Electronic structure calculations

Figure 5 presents the calculated electronic structure of BaFe_2Al_9 and BaCo_2Al_9 from DFT. Panel 5a provides a comparison of the density of states between the two compounds. The shaded region represents the d-orbital contribution at each energy. The d-states are shifted

to lower energies in the Co compound dramatically reducing the density of states at the Fermi energy (dashed line).

The band structure in Fig. 5b shows more detail of these changes. The thicker bands have more transition-metal d-orbital character and the color denotes the contribution from each d-orbital variety. Thinner bands are generally dominated by Al s- and p-orbitals in the depicted energy range.

Note the common features between the two compounds. The thicker d-orbital bands show small dispersion in $\Gamma - M - K$ and $A - L - H$ planes but they are shifted down by 0.7-0.9 eV in the Co compound. Critically, in BaFe_2Al_9 several of the bands at the Fermi level (dashed line) have d-orbital character; the red ($d_{xy}/d_{x^2-y^2}$) bands in the $\Gamma - M - K$ plane and green (d_{xz}/d_{yz}) bands on the $\Gamma - A$ line. In the BaCo_2Al_9 , only thin lines representing Al-dominated bands lie at the Fermi level.

We propose that the partly filled d-bands play an important role in the formation of the CDW in BaFe_2Al_9 . First, this is the most conspicuous difference between the electronic structures in Fig. 5. Second, our physical property measurements suggest that the CDW only opens a gap in some of the bands. In a canonical, single-band CDW system the structural modulation is heralded by a metal-insulator transition. High-temperature metallic properties give way to semiconducting behavior as a band gap opens on cooling.⁸ In contrast, BaFe_2Al_9 displays metallic resistance behavior both above and below the transition (Fig. 2b).

In BaFe_2Al_9 many bands cross the Fermi energy. CDW formation likely gaps out some of these bands (maybe the d-bands) which reduces the density of states. This reduction of metallic carriers causes the abrupt increase in the resistance on cooling but the un-gapped bands facilitate metallic resistance vs. temperature behavior at low temperatures. The magnetic susceptibility data presented in Fig. 2a supports this model. The Pauli paramagnetic contribution to the susceptibility is proportional to the density of states at the Fermi level.⁴⁹ Gap formation on some of the bands by the CDW leads to a smaller density of states and, therefore a weaker Pauli paramagnetic response at low temperature.

We believe the role of the d-orbitals in the CDW we propose is testable. Once the modulated structure of the CDW in BaFe_2Al_9 is determined, the electronic structure can be calculated for the superstructure. Based on our model, we would anticipate that Fe-dominated states would be gapped at the Fermi level and bands from the Al-network would not. This observation would emphasize the relative involvement of these d-orbital states in the structural modulation.

Vajenine and Hoffmann noted something curious about this BaFe_2Al_9 family of compounds; the transition metal is the most electronegative constituent.³⁹ They suggest that Fe and Co will have filled d-orbitals and the remaining electrons are distributed on the Al-network. Our DFT results reveal that this is not quite the case in BaFe_2Al_9 . As we noted above, the d-bands have unfilled states. Their argument still has merit in that the additional electrons per formula unit (F.U.) in BaCo_2Al_9 preferentially fill the d-bands. The thinner bands, with strong Al character, shift less than the d-bands between the two compounds in Fig. 5b. Al-bands fall by 0.15-0.4 eV while the d-bands fall by 0.7-0.9 eV. The smaller shift of Al-network bands is exemplified by the thin hole band above the Fermi energy at the *A* point in both compounds.

This disparate energy shift of the d- and Al-bands suggests that filled d-orbitals are indeed favored in this family of compounds. Unfilled d-orbitals in BaFe_2Al_9 may explain its abrupt volume change at the CDW transition. To fill the Fe d-orbitals, the electrons would have to come from the Al-network. Reducing the filling of the Al-bands would modify network bonding leading to the changes of the lattice parameters presented in Fig. 2d.

The archetypal CDW compounds are characterized by weakly coupled chains or sheets such as NbSe_3 , $\text{K}_{0.3}\text{MoO}_3$, the *RNiC*₂-family, $\text{K}_2\text{Mo}_{15}\text{Se}_{13}$, NbSe_2 , and $(\text{K},\text{Ba})\text{AgTe}_2$.^{8,55-58} CDWs in intermetallic compounds with 3D structural networks, like BaFe_2Al_9 , are notably less common. Examples include a few transition metal silicides, germanides, stannides, and chalcogenides such as $R_2M_3\text{Si}_5$,⁵⁹⁻⁶¹ $R_2M_3\text{Ge}_5$,⁶² and $R_5M_4\text{Si}_{10}$,⁶³⁻⁶⁶ the $\text{Sr}_3\text{Ir}_4\text{Sn}_{13}$ -family^{67,68} and $\text{Ir}_2\text{In}_8\text{Se}$.⁶⁹ Few compounds show first-order CDW transitions like that in

BaFe₂Al₉. Examples include Lu₂Ir₃Si₅, Er₂Ir₃Si₅^{59,60} and light rare-earth variants of *RPt*₂Si₂.⁷⁰ The first two compounds show similar jumps in resistance vs temperature with low temperature metallic behavior like BaFe₂Al₉. Although charge order has been identified in two iron oxides (LuFe₂O₄⁷¹ and magnetite⁷²), BaFe₂Al₉ is the first example of a CDW in an Fe-based compound we are aware of without magnetism.

Identifying a CDW ground-state in BaFe₂Al₉ begs two key questions. First, iron is renowned for its magnetism and partially filled d-orbitals are critical ingredients for magnetic order.⁴⁹ This is particularly true for 3d transition-metal compounds. Therefore, it is somewhat surprising to find a CDW in BaFe₂Al₉ despite its nearly filled Fe d-bands. Why is a charge modulation favored over magnetism in this compound?

Second, the majority of charge density wave transitions are second-order or weakly first order.⁸ In contrast, the CDW in BaFe₂Al₉ appears at a strongly first-order transition with a 1.5% shrinkage along *c*. Why is the CDW transition first order in this compound? What is the role of the large lattice strain that accompanies it?

In general, the mechanism that drives CDW transitions is not entirely clear.^{8,14} This is especially true in materials with relatively 3D electronic structures and many Fermi surfaces, like BaFe₂Al₉. Although Fermi surface nesting is frequently discussed as driving CDW formation, this argument is strongest in materials with particularly 1D character. Electron correlations and wavelength-dependent electron-phonon coupling may be more important in 3D materials like BaFe₂Al₉.

This compound offers a unique opportunity for chemical tuning to explore the origin of its CDW order. First, unlike the more common second-order CDW transition, the first-order transition produces a strong signal for tracking changes. Magnetic susceptibility, resistance, and particularly the lattice parameters all show dramatic discontinuities. This will allow us to easily track the phase transition as we modify the material. Next, BaFe₂Al₉ belongs to a family with some compositional flexibility.³⁹ As a result, this compound offers several opportunities for chemical substitution. Isovalent doping of Sr for Ba, Ru for Fe, or Ga for

Al allow tuning of the lattice size and disorder. The role of band filling could be explored by replacing Fe with other transition metals. Overall, BaFe_2Al_9 has a wonderful potential for tuning its conspicuous first-order CDW transition to learn what drives it.

In summary, we grew crystals of BaFe_2Al_9 and BaCo_2Al_9 from aluminum flux and characterized their temperature-dependent physical properties. These results reveal no transitions in BaCo_2Al_9 and a first-order phase transition in the Fe compound near 100 K. Diffraction results reveal a discontinuous change in lattice parameters across the transition. This strain is large enough to physically shatter the crystals. Single crystal x-ray diffraction revealed the low-temperature phase in BaFe_2Al_9 to be a charge density wave (CDW) with modulated Fe and Ba positions. Comparing the electronic structures of BaFe_2Al_9 and BaCo_2Al_9 hints that the CDW in the former might be associated with Fe d-bands at the Fermi energy. BaFe_2Al_9 offers many opportunities for chemical tuning to answer some outstanding questions about its unusual CDW ground state.

Acknowledgement

We would like to thank Anna Böhmer, Andreas Kreyssig, Joe Paddison, Andrew May, Ji-qi Yang, Gordon Miller, Tom Roberson and Rob Moore for their discussions and insights. We would also like to thank Václav Petříček for his assistance with the modulated structure which required an early copy of Jana2020.

Research supported by the U. S. Department of Energy, Office of Science, Basic Energy Sciences, Materials Sciences and Engineering Division (under contract number DE-AC05-00OR22725). GDS was supported as part of the Energy Dissipation to Defect Evolution (EDDE), an Energy Frontier Research Center funded by the US Department of Energy, Office of Science, Basic Energy Sciences under Contract Number DE-AC05-00OR22725. This research used resources at the Spallation Neutron Source, a DOE Office of Science User Facility operated by Oak Ridge National Laboratory.

Supporting Information Available

The following files are available free of charge.

- CDW_in_BaFe₂Al₉_SI_02.pdf : Details of neutron powder diffraction refinements and Mössbauer fits
- BaFe₂Al₉_neutron_300K_submit.cif : Refined structure of BaFe₂Al₉ at 300 K using neutron diffraction

Supplemental Information

Neutron powder diffraction refinement

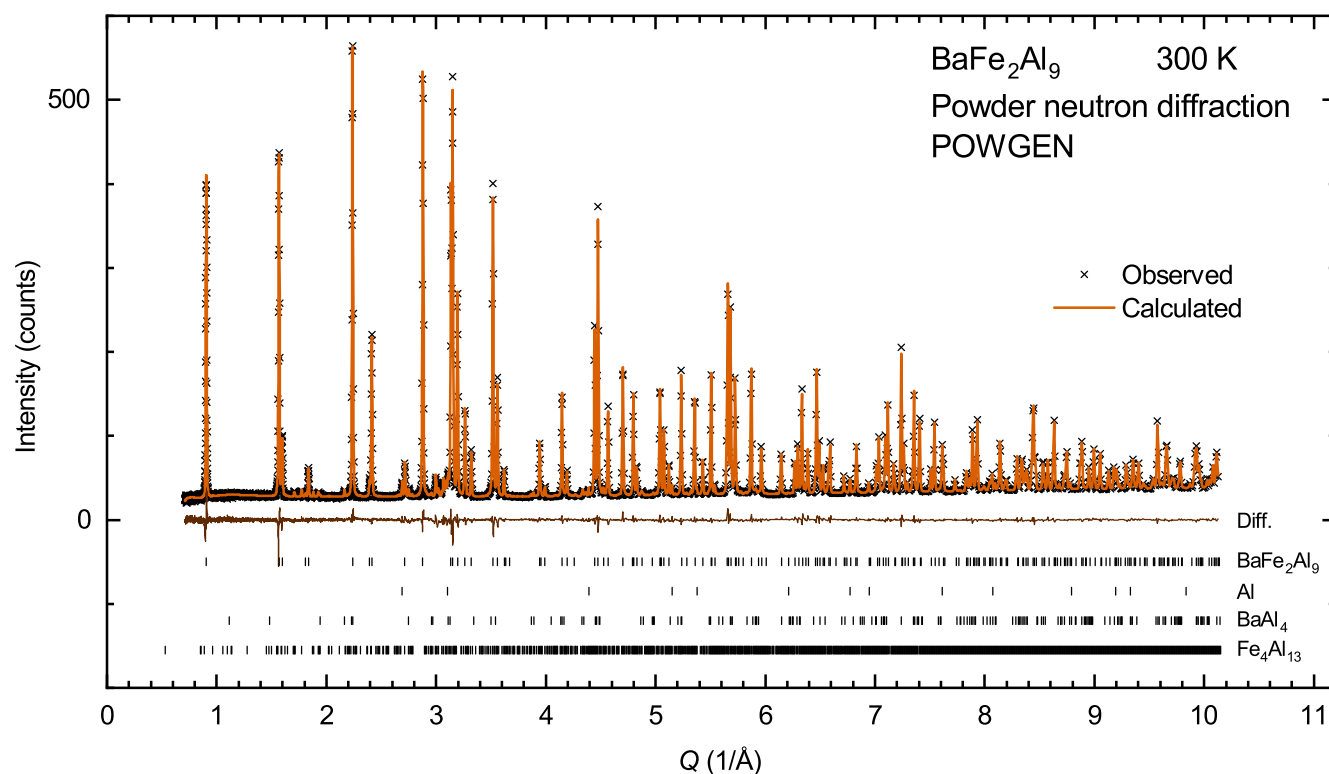


Figure 6: Fit of the 300 K neutron powder diffraction data taken at POWGEN.

Figure 6 depicts the fit to the powder neutron diffraction of BaFe_2Al_9 taken at 300 K. We were not selective with the crystals chosen to grind into the 1.83 g sample. As a result, this measurement represents a worst-case scenario for impurities. The refinement indicates 92.2(3) wt% BaFe_2Al_9 , 1.14(7) wt% Al metal, 2.62(19) wt% BaAl_4 , and 4.00(12) wt% $\text{Fe}_4\text{Al}_{13}$.

Table 1 presents the details of the structure refinement from the powder neutron diffraction data of BaFe₂Al₉ above and below the charge density wave (CDW) transition. Although the compound has a CDW modulation at 50 and 7K the same structure model was used for all temperatures. This was done because no super-lattice peaks are observed in the neutron data to refine a modulated structure. We were able to infer the presence of a CDW modulation in the average structure based on the atomic parameters in Tables 2 and 3. As discussed in the main text, the anisotropic atomic displacement parameters (ADPs) show an anomalous temperature dependence below 100K consistent with the CDW model we propose.

Our refinement indicated that the Fe site in BaFe₂Al₉ mostly occupied with only a few percent vacancies. This reduced site occupancy was also observed when x-ray data were refined.

Table 1: Neutron powder refinement details from POWGEN time of flight data.

Chemical formula	BaFe _{1.92} Al ₉			
Formula wt. (g/molF.U.)	487.383			
Crystal system	hexagonal			
Space group	<i>P6/mmm</i> (191)			
Temperature (K)	300	120	50	7
<i>a</i> (Å)	8.018667(16)	8.006172(15)	8.04357(3)	8.04363(3)
<i>c</i> (Å)	3.934816(14)	3.929166(13)	3.86933(3)	3.86835(3)
<i>V</i> (Å ³)	219.1086(10)	218.1127(9)	216.8024(19)	216.7509(18)
<i>Z</i>	1			
Density calculated (g/cm ³)	3.7277	3.7447	3.7674	3.7683
wavelength range (Å)	0.97 - 2.033			
F(000)	494.718	494.718	482.026	494.718
Time of flight range (ms)	11.3 - 315			
No. of variables	46			
RF(obs)	1.15	1.17	2.7	2.65
RFw(obs)	1.58	1.69	4.4	4.15
Goodness of fit	2.8	3	4.58	4.27
Absorption	0.077(2)	0.077(2)	0.078(4)	0.074(3)

Mössbauer fits

In the results section we note an inconsistency between our Mössbauer spectra from

Table 2: Neutron refinement BaFe₂Al₉ atomic parameters

Atom	Site	x	y	z	$U_{aniso.}$	Occupancy
300 K						
Al1	3 <i>f</i>	$\frac{1}{2}$	0	0	0.0099(2)	1
Al2	6 <i>m</i>	0.21481(4)	0.42961(8)	$\frac{1}{2}$	0.0089(2)	1
Ba	1 <i>a</i>	0	0	0	0.0126(3)	1
Fe	2 <i>c</i>	$\frac{1}{3}$	$\frac{2}{3}$	0	0.0067(1)	0.984(3)
120 K						
Al1	3 <i>f</i>	$\frac{1}{2}$	0	0	0.0059(2)	1
Al2	6 <i>m</i>	0.21484(4)	0.42968(8)	$\frac{1}{2}$	0.0055(2)	1
Ba	1 <i>a</i>	0	0	0	0.0064(2)	1
Fe	2 <i>c</i>	$\frac{1}{3}$	$\frac{2}{3}$	0	0.0045(1)	0.985(3)
50 K						
Al1	3 <i>f</i>	$\frac{1}{2}$	0	0	0.0055(4)	1
Al2	6 <i>m</i>	0.21355(7)	0.42711(13)	$\frac{1}{2}$	0.0077(3)	1
Ba	1 <i>a</i>	0	0	0	0.0101(4)	1
Fe	2 <i>c</i>	$\frac{1}{3}$	$\frac{2}{3}$	0	0.0127(2)	0.988(5)
7 K						
Al1	3 <i>f</i>	$\frac{1}{2}$	0	0	0.0053(3)	1
Al2	6 <i>m</i>	0.21354(6)	0.42707(12)	$\frac{1}{2}$	0.0076(3)	1
Ba	1 <i>a</i>	0	0	0	0.0093(4)	1
Fe	2 <i>c</i>	$\frac{1}{3}$	$\frac{2}{3}$	0	0.0125(2)	0.985(5)

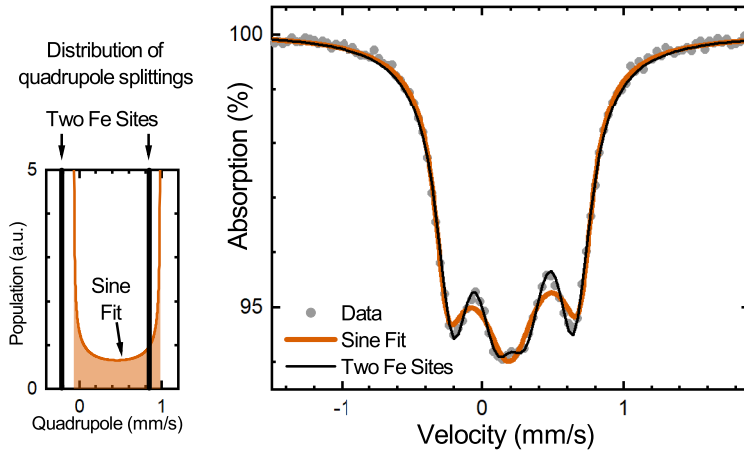


Figure 7: Fits of ⁵⁴ Mössbauer spectra from BaFe₂Al₉ in the charge density wave phase at 15 K. The left panel shows the distribution of quadrupole parameters for two Fe sites model (black) and the sine-modulated quadrupole model that best fit the spectra. The right hand plot shows that two-site model (black) fits the measured spectra (gray points) better than the sine modulated model (orange).

Table 3: Neutron refinement BaFe₂Al₉ atomic displacement parameters

Atom	U_{11}	U_{22}	U_{33}	U_{12}
300 K				
Al1	0.0128(3)	0.0071(4)	0.0078(4)	0.00356(18)
Al2	0.0093(2)	0.0105(2)	0.0073(3)	0.00525(12)
Ba	0.0156(3)	0.0156(3)	0.0067(5)	0.00782(17)
Fe	0.00598(15)	0.00598(15)	0.00898(19)	0.00299(7)
120 K				
Al1	0.0073(3)	0.0056(3)	0.0043(3)	0.00282(17)
Al2	0.00589(19)	0.0069(2)	0.0040(3)	0.00344(11)
Ba	0.0083(3)	0.0083(3)	0.0026(4)	0.00414(14)
Fe	0.00389(14)	0.00389(14)	0.00570(17)	0.00195(7)
50 K				
Al1	0.0049(4)	0.0045(5)	0.0069(6)	0.0022(3)
Al2	0.0064(3)	0.0107(4)	0.0073(5)	0.0054(2)
Ba	0.0125(5)	0.0125(5)	0.0052(7)	0.0063(2)
Fe	0.0038(3)	0.0038(3)	0.0305(4)	0.00188(13)
7 K				
Al1	0.0048(4)	0.0046(5)	0.0064(5)	0.0023(2)
Al2	0.0064(3)	0.0108(4)	0.0070(4)	0.00539(19)
Ba	0.0118(4)	0.0118(4)	0.0044(7)	0.0059(2)
Fe	0.0035(2)	0.0035(2)	0.0305(4)	0.00176(12)

BaFe₂Al₉ and the charge density wave modulation presented in Fig. 3d. Specifically, the observed super-lattice reflections from single crystal x-ray diffraction signal a simple sine-modulation of the atomic positions. This should give a distribution of Fe atom environments with a range of Mössbauer parameters. For example, a sine-modulation of the quadrupole parameter would yield the orange distribution of values in the left panel of Fig. 7. This contrasts with the discrete pair of values from a fit to the two Fe-site model (thick black line).

We tried to fit the low temperature Mössbauer spectra of BaFe₂Al₉ with such a modulated model. We summed the spectra of 20 sites with sine-modulated Mössbauer parameters. The maximum and minimum values of the quadrupole splitting, isomer shift and linewidth were allowed to vary and the best fit is given by the orange curve on the right-hand plot of Fig. 7. This fit is distinctly worse than the two iron site model in black presented in the main text.

References

- (1) Momma, K.; Izumi, F. VESTA3 for three-dimensional visualization of crystal, volumetric and morphology data. *Journal of Applied Crystallography* **2011**, *44*, 1272–1276.
- (2) Bhadeshia, H. K. D. H.; Honeycombe, R. W. K. *Steels : microstructure and properties*; Elsevier, Butterworth-Heinemann: Amsterdam, 2006.
- (3) Orikasa, Y.; Maeda, T.; Koyama, Y.; Murayama, H.; Fukuda, K.; Tanida, H.; Arai, H.; Matsubara, E.; Uchimoto, Y.; Ogumi, Z. Transient phase change in two phase reaction between LiFePO₄ and FePO₄ under battery operation. *Chemistry of Materials* **2013**, *25*, 1032–1039.
- (4) Yahia, H. B.; Shikano, M.; Kobayashi, H. Phase transition mechanisms in Li_xCoO₂ (0.25 ≤ x ≤ 1) based on group-subgroup transformations. *Chemistry of Materials* **2013**, *25*, 3687–3701.

- (5) Tomforde, J.; Bensch, W.; Kienle, L.; Duppel, V.; Merkelbach, P.; Wuttig, M. Thin films of Ge-Sb-Te-based phase change materials: microstructure and in situ transformation. *Chemistry of Materials* **2011**, *23*, 3871–3878.
- (6) Bischoff, F.; Auwärter, W.; Barth, J. V.; Schiffrin, A.; Fuhrer, M.; Weber, B. Nanoscale phase engineering of niobium diselenide. *Chemistry of Materials* **2017**, *29*, 9907–9914.
- (7) Meddar, L.; Josse, M.; Maglione, M.; Guiet, A.; La, C.; Deniard, P.; Decourt, R.; Lee, C.; Tian, C.; Jobic, S.; Whangbo, M.-H.; Payen, C. Increasing the phase-transition temperatures in spin-frustrated multiferroic MnWO_4 by Mo doping. *Chemistry of Materials* **2012**, *24*, 353–360.
- (8) Grüner, G. *Density waves in solids*; Perseus Publishing, Cambridge, Mass., 1994.
- (9) Burdett, J. *Chemical bonding in solids*; Oxford University Press: New York, NY, 1995.
- (10) Hoffmann, R. How chemistry and physics meet in the solid state. *Angewandte Chemie International Edition in English* **1987**, *26*, 846–878.
- (11) Owens-Baird, B.; Xu, J.; Petrovykh, D. Y.; Bondarchuk, O.; Ziouani, Y.; González-Ballesteros, N.; Yox, P.; Sapountzi, F. M.; Niemantsverdriet, H.; Kolen'ko, Y. V.; Kovnir, K. NiP_2 : A story of two divergent polymorphic multifunctional materials. *Chemistry of Materials* **2019**, *31*, 3407–3418.
- (12) Kobayashi, S.; Katayama, N.; Manjo, T.; Ueda, H.; Michioka, C.; Sugiyama, J.; Sassa, Y.; Forslund, O. K.; Månsson, M.; Yoshimura, K.; Sawa, H. Linear trimer formation with antiferromagnetic ordering in 1T-CrSe₂ originating from Peierls-like instabilities and interlayer Se-Se Interactions. *Inorganic Chemistry* **2019**, *58*, 14304–14315.
- (13) Alemany, P.; Lluell, M.; Canadell, E. Host-guest interactions, uniform vs fragmented

- linear atom chains and likeliness of Peierls distortions in the $(\text{Ca}_7\text{N}_4)[M_x]$ ($M = \text{Ag}, \text{Ga}, \text{In}$) phases. *Inorganic Chemistry* **2009**, *48*, 2919–2931.
- (14) Zhu, X.; Guo, J.; Zhang, J.; Plummer, E. W. Misconceptions associated with the origin of charge density waves. *Advances in Physics: X* **2017**, *2*, 622–640.
- (15) Grüner, G. The dynamics of charge-density waves. *Reviews of Modern Physics* **1988**, *60*, 1129–1181.
- (16) Johannes, M. D.; Mazin, I. I. Fermi surface nesting and the origin of charge density waves in metals. *Physical Review B* **2008**, *77*, 165135.
- (17) Chikina, A.; Fedorov, A.; Bhoi, D.; Voroshnin, V.; Haubold, E.; Kushnirenko, Y.; Kim, K. H.; Borisenko, S. Turning charge-density waves into Cooper pairs. *npj Quantum Materials* **2020**, *5*, 22.
- (18) Chen, C.-W.; Choe, J.; Morosan, E. Charge density waves in strongly correlated electron systems. *Reports on Progress in Physics* **2016**, *79*, 084505.
- (19) Duvjir, G. et al. Emergence of a metal-insulator transition and high-temperature charge-density waves in VSe_2 at the monolayer limit. *Nano Letters* **2018**, *18*, 5432–5438.
- (20) Malliakas, C. D.; Kanatzidis, M. G. Nb-Nb interactions define the charge density wave structure of 2H-NbSe_2 . *Journal of the American Chemical Society* **2013**, *135*, 1719–1722.
- (21) Duong, D. L.; Ryu, G.; Hoyer, A.; Lin, C.; Burghard, M.; Kern, K. Raman characterization of the charge density wave phase of 1T-TiSe_2 : From bulk to atomically thin layers. *ACS Nano* **2017**, *11*, 1034–1040.
- (22) Wilson, J. A.; Salvo, F. J. D.; Mahajan, S. Charge-density waves and superlattices in

- the metallic layered transition metal dichalcogenides. *Advances in Physics* **1975**, *24*, 117–201.
- (23) Rossnagel, K. On the origin of charge-density waves in select layered transition-metal dichalcogenides. *Journal of Physics: Condensed Matter* **2011**, *23*, 213001.
- (24) Bianco, R.; Errea, I.; Monacelli, L.; Calandra, M.; Mauri, F. Quantum enhancement of charge density wave in NbS₂ in the two-dimensional limit. *Nano Letters* **2019**, *19*, 3098–3103.
- (25) Fu, W.; Chen, Y.; Lin, J.; Wang, X.; Zeng, Q.; Zhou, J.; Zheng, L.; Wang, H.; He, Y.; He, H.; Fu, Q.; Suenaga, K.; Yu, T.; Liu, Z. Controlled synthesis of atomically thin 1T-TaS₂ for tunable charge density wave phase transitions. *Chemistry of Materials* **2016**, *28*, 7613–7618.
- (26) Feng, J. et al. Electronic structure and enhanced charge-density wave order of monolayer VSe₂. *Nano Letters* **2018**, *18*, 4493–4499.
- (27) Fumega, A. O.; Phillips, J.; Pardo, V. Controlled two-dimensional ferromagnetism in 1T-CrTe₂: The role of charge density wave and strain. *The Journal of Physical Chemistry C* **2020**, *124*, 21047–21053.
- (28) Xi, X.; Zhao, L.; Wang, Z.; Berger, H.; Forró, L.; Shan, J.; Mak, K. F. Strongly enhanced charge-density-wave order in monolayer NbSe₂. *Nature Nanotechnology* **2015**, *10*, 765–769.
- (29) Whangbo, M. H.; Gressier, P. Characterization of the charge density waves in niobium triselenide (NbSe₃) by band electronic structure. *Inorganic Chemistry* **1984**, *23*, 1305–1306.
- (30) Hor, Y. S.; Xiao, Z. L.; Welp, U.; Ito, Y.; Mitchell, J. F.; Cook, R. E.; Kwok, W. K.;

- Crabtree, G. W. Nanowires and nanoribbons of charge-density-wave conductor NbSe₃. *Nano Letters* **2005**, *5*, 397–401.
- (31) Weber, F.; Rosenkranz, S.; Castellan, J.-P.; Osborn, R.; Hott, R.; Heid, R.; Bohnen, K.-P.; Egami, T.; Said, A. H.; Reznik, D. Extended phonon collapse and the origin of the charge-density wave in 2H-NbSe₂. *Physical Review Letters* **2011**, *107*, 107403.
- (32) Arguello, C. J.; Chockalingam, S. P.; Rosenthal, E. P.; Zhao, L.; Gutiérrez, C.; Kang, J. H.; Chung, W. C.; Fernandes, R. M.; Jia, S.; Millis, A. J.; Cava, R. J.; Pasupathy, A. N. Visualizing the charge density wave transition in 2H-NbSe₂ in real space. *Physical Review B* **2014**, *89*, 235115.
- (33) Shimomura, S.; Murao, H.; Tsutsui, S.; Nakao, H.; Nakamura, A.; Hedo, M.; Nakama, T.; Ōnuki, Y. Lattice modulation and structural phase transition in the anti-ferromagnet EuAl₄. *Journal of the Physical Society of Japan* **2019**, *88*, 014602.
- (34) Turban, K.; Schäfer, H. Zur kenntnis des BaFe₂Al₉-strukturtyps: Ternäre aluminide AT₂Al₉ MIT A = Ba, Sr und T = Fe, Co, Ni. *Journal of the Less Common Metals* **1975**, *40*, 91–96.
- (35) Manyako, I. B.; Yanson, T. I.; Zarechnyuk, O. S. Phase equilibria in the Ca-Co(Ni)-Al systems at 700 K. *Izv. Akad. Nauk SSSR, Met.* **1988**, *3*, 185–188.
- (36) Thiede, V. M. T.; Jeitschko, W. Crystal structure of europium cobalt aluminide (1/2/9), EuCo₂Al₉. *Zeitschrift für Kristallographie - New Crystal Structures* **1999**, *214*, 149–150.
- (37) Lei, X.-W.; Zhong, G.-H.; Li, L.-H.; Hu, C.-L.; Li, M.-J.; Mao, J.-G. Eu₃Co₂In₁₅ and KM₂In₉ (M = Co, Ni): 3D frameworks based on transition metal centered In₉ clusters. *Inorganic Chemistry* **2009**, *48*, 2526–2533.

- (38) Calta, N. P.; Han, F.; Kanatzidis, M. G. Synthesis, structure, and rigid unit mode-like anisotropic thermal expansion of BaIr_2In_9 . *Inorganic Chemistry* **2015**, *54*, 8794–8799.
- (39) Vajenine, G. V.; Hoffmann, R. Magic electron counts for networks of condensed clusters: Vertex-sharing aluminum octahedra. *Journal of the American Chemical Society* **1998**, *120*, 4200–4208.
- (40) Bergerhoff, G.; Brown, I. D. Crystallographic databases. *International Union of Crystallography, Chester* **1987**, *360*, 77–95.
- (41) Jain, A.; Ong, S. P.; Hautier, G.; Chen, W.; Richards, W. D.; Dacek, S.; Cholia, S.; Gunter, D.; Skinner, D.; Ceder, G.; Persson, K. A. Commentary: The Materials Project: A materials genome approach to accelerating materials innovation. *APL Materials* **2013**, *1*, 011002.
- (42) Canfield, P. C.; Kong, T.; Kaluarachchi, U. S.; Jo, N. H. Use of frit-disc crucibles for routine and exploratory solution growth of single crystalline samples. *Philosophical Magazine* **2016**, *96*, 84–92.
- (43) Huq, A.; Kirkham, M.; Peterson, P. F.; Hodges, J. P.; Whitfield, P. S.; Page, K.; Húgle, T.; Iverson, E. B.; Parizzi, A.; Rennich, G. POWGEN: rebuild of a third-generation powder diffractometer at the Spallation Neutron Source. *Journal of Applied Crystallography* **2019**, *52*, 1189–1201.
- (44) Petříček, V.; Dušek, M.; Palatinus, L. Crystallographic computing system JANA2006: general features. *Zeitschrift für Kristallographie - Crystalline Materials* **2014**, *229*, 345.
- (45) CrysAlisPRO. Oxford Diffraction/Agilent Technologies UK Ltd, Yarnton, England.
- (46) Kresse, G.; Joubert, D. From ultrasoft pseudopotentials to the projector augmented-wave method. *Physical Review B* **1999**, *59*, 1758–1775.

- (47) Perdew, J. P.; Burke, K.; Ernzerhof, M. Generalized gradient approximation made simple. *Physical Review Letters* **1996**, *77*, 3865–3868.
- (48) Kresse, G.; Furthmüller, J. Efficiency of ab-initio total energy calculations for metals and semiconductors using a plane-wave basis set. *Computational Materials Science* **1996**, *6*, 15–50.
- (49) Blundell, S. *Magnetism in condensed matter*; Oxford University Press, USA, 2001.
- (50) Kittel, C. *Introduction to solid state physics*, eighth ed.; John Wiley & Sons Inc: Hoboken, NJ, 2004.
- (51) Ryżyńska, Z.; Klimczuk, T.; Winiarski, M. J. Single crystal growth and physical properties of $M\text{Co}_2\text{Al}_9$ ($M = \text{Sr}, \text{Ba}$). *Journal of Solid State Chemistry* **2020**, *289*, 121509.
- (52) Stokes, H. T.; Hatch, D. M.; Campbell, B. J. ISODISTORT, ISOTROPY software suite, version 6.7.2. Sep 2020; iso.byu.edu.
- (53) Campbell, B. J.; Stokes, H. T.; Tanner, D. E.; Hatch, D. M. ISODISPLACE: a web-based tool for exploring structural distortions. *Journal of Applied Crystallography* **2006**, *39*, 607–614.
- (54) Boucher, F.; Evain, M.; Petříček, V. Incommensurately modulated structure of $\text{TaGe}_{0.354}\text{Te}_2$: application of crenel functions. *Acta Crystallographica Section B Structural Science* **1996**, *52*, 100–109.
- (55) Steiner, S.; Michor, H.; Sologub, O.; Hinterleitner, B.; Höfenstock, F.; Waas, M.; Bauer, E.; Stöger, B.; Babizhetskyy, V.; Levytskyy, V.; Kotur, B. Single-crystal study of the charge density wave metal LuNiC_2 . *Physical Review B* **2018**, *97*, 205115.
- (56) Roman, M.; Strychalska-Nowak, J.; Klimczuk, T.; Kolincio, K. K. Extended phase diagram of RNiC_2 family: Linear scaling of the Peierls temperature. *Physical Review B* **2018**, *97*, 041103.

- (57) Candolfi, C.; Míšek, M.; Gougeon, P.; Orabi, R. A. R. A.; Gall, P.; Gautier, R.; Migot, S.; Ghanbaja, J.; Kaštil, J.; Levinský, P.; Hejtmánek, J.; Dauscher, A.; Malaman, B.; Lenoir, B. Coexistence of a charge density wave and superconductivity in the cluster compound $\text{K}_2\text{Mo}_{15}\text{Se}_{19}$. *Physical Review B* **2020**, *101*, 134521.
- (58) Gourdon, O.; Hanko, J.; Boucher, F.; Petricek, V.; Whangbo, M.-H.; Kanatzidis, M. G.; Evain, M. A unique distortion in $\text{K}_{1/3}\text{Ba}_{2/3}\text{AgTe}_2$: X-ray diffraction determination and electronic band structure analysis of its incommensurately modulated structure. *Inorganic Chemistry* **2000**, *39*, 1398–1409.
- (59) Ramakrishnan, S.; Schönleber, A.; Rekiş, T.; van Well, N.; Noohinejad, L.; van Smaalen, S.; Tolkiehn, M.; Paulmann, C.; Bag, B.; Thamizhavel, A.; Pal, D.; Ramakrishnan, S. Unusual charge density wave transition and absence of magnetic ordering in $\text{Er}_2\text{Ir}_3\text{Si}_5$. *Physical Review B* **2020**, *101*, 060101.
- (60) Singh, Y.; Pal, D.; Ramakrishnan, S.; Awasthi, A. M.; Malik, S. K. Phase transitions in $\text{Lu}_2\text{Ir}_3\text{Si}_5$. *Physical Review B* **2005**, *71*, 045109.
- (61) Sangeetha, N. S.; Thamizhavel, A.; Tomy, C. V.; Basu, S.; Awasthi, A. M.; Ramakrishnan, S.; Pal, D. Interplay of superconductivity and charge density wave ordering in pseudoternary alloy compounds: $\text{Lu}_2\text{Ir}_3(\text{Si}_{1-x}\text{Ge}_x)_5$, $\text{Lu}_2(\text{Ir}_{1-x}\text{Rh}_x)_3\text{Si}_5$, and $(\text{Lu}_{1-x}\text{Sc}_x)_2\text{Ir}_3\text{Si}_5$. *Physical Review B* **2012**, *86*, 024524.
- (62) Bugaris, D. E.; Malliakas, C. D.; Han, F.; Calta, N. P.; Sturza, M.; Krogstad, M. J.; Osborn, R.; Rosenkranz, S.; Ruff, J. P. C.; Trimarchi, G.; Bud'ko, S. L.; Balasubramanian, M.; Chung, D. Y.; Kanatzidis, M. G. Charge density wave in the new polymorphs of $\text{RE}_2\text{Ru}_3\text{Ge}_5$ (RE = Pr, Sm, Dy). *Journal of the American Chemical Society* **2017**, *139*, 4130–4143.
- (63) Kuo, Y.-K.; Lue, C. S.; Hsu, F. H.; Li, H. H.; Yang, H. D. Thermal properties of $\text{Lu}_5\text{Ir}_4\text{Si}_{10}$ near the charge-density-wave transition. *Physical Review B* **2001**, *64*, 125124.

- (64) Kuo, Y.-K.; Hsu, F. H.; Li, H. H.; Huang, H. L.; Huang, C. W.; Lue, C. S.; Yang, H. D. Ionic size and atomic disorder effects on the charge-density-wave transitions in $R_5\text{Ir}_4\text{Si}_{10}$ ($R = \text{Dy-Lu}$). *Physical Review B* **2003**, *67*, 195101.
- (65) Lue, C. S.; Kuo, Y.-K.; Hsu, F. H.; Li, H. H.; Yang, H. D.; Fodor, P. S.; Wenger, L. E. Thermal hysteresis in the charge-density-wave transition of $\text{Lu}_5\text{Rh}_4\text{Si}_{10}$. *Physical Review B* **2002**, *66*, 033101.
- (66) Yang, H. D.; Klavins, P.; Shelton, R. N. Phase transitions in the superconducting compound $\text{Lu}_5\text{Rh}_4\text{Si}_{10}$ at ambient and high pressure. *Physical Review B* **1991**, *43*, 7676–7680.
- (67) Klintberg, L. E.; Goh, S. K.; Alireza, P. L.; Saines, P. J.; Tompsett, D. A.; Logg, P. W.; Yang, J.; Chen, B.; Yoshimura, K.; Grosche, F. M. Pressure- and composition-induced structural quantum phase transition in the cubic superconductor $(\text{Sr,Ca})_3\text{Ir}_4\text{Sn}_{13}$. *Physical Review Letters* **2012**, *109*, 237008.
- (68) Welsch, J.; Ramakrishnan, S.; Eisele, C.; van Well, N.; Schönleber, A.; van Smaalen, S.; Matteppanavar, S.; Thamizhavel, A.; Tolkiehn, M.; Paulmann, C.; Ramakrishnan, S. Second-order charge-density-wave transition in single crystals of $\text{La}_3\text{Co}_4\text{Sn}_{13}$. *Physical Review Materials* **2019**, *3*, 125003.
- (69) Khoury, J. F.; Rettie, A. J. E.; Robredo, I.; Krogstad, M. J.; Malliakas, C. D.; Bergara, A.; Vergniory, M. G.; Osborn, R.; Rosenkranz, S.; Chung, D. Y.; Kanatzidis, M. G. The subchalcogenides $\text{Ir}_2\text{In}_8\text{Q}$ ($Q = \text{S, Se, Te}$): Dirac semimetal candidates with re-entrant structural modulation. *Journal of the American Chemical Society* **2020**, *142*, 6312–6323.
- (70) Nagano, Y.; Araoka, N.; Mitsuda, A.; Yayama, H.; Wada, H.; Ichihara, M.; Isobe, M.; Ueda, Y. Charge density wave and superconductivity of $R\text{Pt}_2\text{Si}_2$ ($R = \text{Y, La, Nd, and Lu}$). *Journal of the Physical Society of Japan* **2013**, *82*, 064715.

- (71) Ikeda, N.; Ohsumi, H.; Ohwada, K.; Ishii, K.; Inami, T.; Kakurai, K.; Murakami, Y.; Yoshii, K.; Mori, S.; Horibe, Y.; Kitô, H. Ferroelectricity from iron valence ordering in the charge-frustrated system LuFe_2O_4 . *Nature* **2005**, *436*, 1136–1138.
- (72) Walz, F. The Verwey transition - a topical review. *Journal of Physics: Condensed Matter* **2002**, *14*, R285–R340.

Graphical TOC Entry

